

## MULTILINE HYDROXYL TAGGING VELOCIMETRY IN REACTING AND NONREACTING EXPERIMENTAL FLOWS

Lubomir A. Ribarov\*, Joseph A. Wehrmeyer+, and Robert W. Pitz‡

Department of Mechanical Engineering

Vanderbilt University, Nashville, TN 37235-1592, USA

(Fax: +1.615.343.6687, E-Mail: robert.w.pitz@vanderbilt.edu)

### Abstract

A new compact micro-lens optical system has been developed to produce a 7 x 7 multiline optical grid for Hydroxyl Tagging Velocimetry (HTV). These lines provide additional spatial information and aid the software tracking of the flowfield by increasing its resolution. Single-photon photodissociation of ground-state H<sub>2</sub>O by a ~193-nm ArF excimer laser “writes” a 7 x 7 beam molecular grid with very long gridlines of superequilibrium OH and H photoproducts in either room air flowfields or in H<sub>2</sub>-Air flames due to the presence of H<sub>2</sub>O vapor. The displaced OH tag lines’ positions are revealed through fluorescence by  $A^2\Sigma^+$  ( $\nu' = 0$ )  $\leftarrow X^2\Pi_i$  ( $\nu'' = 0$ ) OH excitation using a ~308 nm pulsed frequency-doubled dye laser. A time-of-flight software (DaVis 6.0 Stereo PIV/PTV, LaVision, GmbH) determines the instantaneous velocity field. HTV tag lifetime comparisons between experimental results and theoretical predictions are discussed.

### Introduction

Accurate and reliable velocimetry measurements are essential in our understanding of the fluid-mechanical, thermodynamical, and thermo-chemical properties of a given experimental flowfield. There is a need for nonintrusive velocimetry methods, which do not perturb the interrogated flowfield and provide a high degree of accuracy. In recent years several such optical diagnostic methods have been developed. Having found a wide application in aerodynamics, combustion, and fluid dynamics, these methods are intrinsically nonintrusive and thus do not suffer the problems usually associated with insertion devices (e.g. static and total pressure probes, pitot tubes, hot-wire/hot-film anemometers, etc.) used in more traditional measurements.<sup>1</sup>

Laser-based nonintrusive velocity measurements in experimental gas flowfields are performed routinely with molecular velocimetry methods. Unlike the Doppler-shifted molecular velocimetry methods,<sup>2-8</sup> that

tend to be inaccurate at low speeds due to the extremely small shift, molecular tagging methods can be applied to a wide range of experimental flowfield velocities.

In molecular flow tagging, the specific molecular marker is written into the interrogated gas and velocity is determined by computing the displaced marker’s position over a known time period. Several molecular tagging methods rely on seeding of the gas flow prior to its interrogation by the laser light sources. A detailed description of these methods is found elsewhere.<sup>9</sup> Such molecular methods with chemical additives are often undesirable from an environmental and/or safety aspect, and in large-scale applications they can be prohibitively costly. Excessive buildup of seed particles on test section access windows presents another serious challenge as clearly illustrated in a recent work.<sup>10</sup> In addition, the tracer particles with their large inertia relative to the gas flow molecules (esp. in supersonic flow fields), are often susceptible to flow field irregularities (e.g. shocks, temperature and velocity gradients, etc.) and may not follow accurately the interrogated flow streamlines.<sup>11</sup> Generally, an upper limit on particle size is bound by particle inertia, while the lower limit is dictated by Brownian motion and molecular slip in addition to the decreasing light-scattering cross sections due to the decreased individual particle size.<sup>12</sup> Lorentz-Mie scattering from the seed particles also interferes with simultaneous diagnostics at- or near- the excitation wavelength. Other forces that can similarly cause the motion of the particles to deviate from the interrogated fluid motion (although to a lesser degree) include gravitational, centrifugal, acoustic, diffusiophoretic, photophoretic, phosphoretic, and thermophoretic.<sup>13,14</sup> This leads to undesirable inaccuracies in the velocity measurements. Finally, thermophoretic forces in temperature gradients (e.g. in combustion environments) can bias the velocity measurement.<sup>15</sup>

Time-of-flight (TOF) unseeded molecular flow tagging velocimetry methods have been successfully developed such as two-photon water vapor dissociation,<sup>16</sup> Raman excitation + laser-induced electronic fluorescence (RELIEF) of O<sub>2</sub>,<sup>17</sup> and ozone tagging velocimetry (OTV).<sup>18</sup> Nonlinear methods<sup>16,17</sup> generally produce shorter lines due to the signal’s inverse dependence on the square of beam diameter. Elevated temperatures can be detrimental to some

\* Student Member AIAA

+ Senior Member AIAA

‡ Associate Fellow AIAA, Corresponding Author

This material is declared a work of the U.S.

Government and is not subject to copyright protection in the United States.

unseeded tagging methods,<sup>17,18</sup> and have led to the development of other nonintrusive molecular methods (HTV) amenable to either low-<sup>9</sup> or high-temperature reacting flows.<sup>19,20</sup>

In this work, a frequency-doubled dye laser pumped by an Nd-YAG laser (also frequency-doubled) is used as a “read” source to demonstrate HTV’s applicability to low- and high-temperature flowfields. By operating the frequency-doubled dye at ~308 nm, the vibrational transitions of the  $A^2\Sigma^+ (v' = 0) \leftarrow X^2\Pi_i (v'' = 0)$  OH band are accessed. These  $(0 \leftarrow 0)$  transitions result in fluorescence that is about two orders of magnitude (where the ratio of the Einstein “B” coefficients for  $(0 \leftarrow 0)$  and  $(3 \leftarrow 0)$  respectively is  $B_{00}/B_{30} \cong 167$ )<sup>21</sup> stronger than that for the  $(3 \leftarrow 0)$  transitions previously used for some of some earlier HTV work.<sup>19,20</sup> These strongly fluorescing OH  $(0 \leftarrow 0)$  transitions compensate for the relatively weak 193 nm photodissociation cross-section of ground vibrational state  $H_2O$ ,<sup>19,20,22</sup> allowing HTV to be applied to low temperature (300 K) flowfields. HTV is also applied in lean  $H_2$ -air flames where pumping of the strongly fluorescing OH  $(0 \leftarrow 0)$  transition is used. A wide range of velocity flowfields (slow- to near-sonic) is successfully interrogated and the results are demonstrated.

### Experimental System

A schematic of the experimental system is shown in Fig. 1. The low temperature HTV demonstration consists of two laser light sources. A tunable Lambda Physik COMPex-150T 193-nm ArF excimer laser is the write laser. The output of the narrowband ArF excimer laser (~150 mJ/pulse, 0.003 nm linewidth, 0.2 mrad divergence at FWHM) is divided into two sets of seven beams formed by two stacks of seven 0.3-m focal length (f.l.) cylindrical micro lenses (20 mm x 3 mm x 3 mm) each. Both sets of laser light beams cross in the flowfield producing a 49-point optical grid. The ArF beams are focused to 0.3 mm beam waists by a second set of 0.3-m f.l. cylindrical lenses (25 mm x 40 mm). The tunable ArF excimer laser is operated in its broadband mode (~1 nm linewidth) since the  $H_2O$  absorption band is a broad continuum lacking any distinct absorption lines.<sup>19</sup> The total distance traveled by each of the ArF grid lines is over 1 m in (unpurged) room air and leads to ~16 % loss (estimated) in energy from laser exit to the measurement zone.

The output of a Continuum Powerlite Nd-YAG laser (532-nm) is frequency-doubled and is used to pump a Continuum ND6000 dye laser whose output is frequency doubled to ~308 nm to provide the (20 mJ/pulse, tunable, 0.05  $cm^{-1}$  bandwidth) read laser. Approximately 5-6 mJ/pulse is lost due to beam transmission losses to the measurement volume. The

308-nm light output of the dye laser is focused by a 1 m f. l. cylindrical lens to a sheet of 20 mm by 0.5 mm cross section. Images from the measurement volume were collected through a multi-element UV imaging lens (Nikon, UV-Nikkor F/4.5,  $f = 105$  mm) coupled to a gated Princeton Instruments ICCD camera (576 x 384 array, 22  $\mu m$  pixels). The gating time was typically 50 ns. A 3-mm thick butyl acetate filter (passing wavelengths longer than 255 nm) was placed in front of the UV lens to reject the strong  $O_2$  fluorescence lines caused by the 193-nm ArF excimer, thus preventing the appearance of  $O_2$  fluoresce on the CCD image from photocathode image persistence.<sup>18</sup> The output of the read dye laser is tuned to excite the strong  $A^2\Sigma^+ (v' = 0) \leftarrow X^2\Pi_i (v'' = 0)$  OH transition.

### OH Tag Spectral Identification and Formation

Figure 2b shows the fluorescence excitation spectrum for the flow tag measured in quiescent room air conditions (297 K, 40% Relative Humidity, RH) for a ~1 nm range of the tunable dye laser. The dye laser does have a wider tuning range; however, to keep the dye laser output relatively strong (and close to its peak value), its range was kept at around 1 nm, between ~307.3 nm (32545  $cm^{-1}$ ) and ~308.2 nm (32445  $cm^{-1}$ ). The dye laser’s output for this range was in the relatively linear section of the laser dye-tuning curve; hence, the laser’s output power was normalized in a linear fashion. The spectral signature of OH-LIF is clearly identified in this excitation and transitions are assigned by comparing the experimental results to earlier spectral data<sup>23,24</sup> as well as to a simulated spectrum (Fig. 2a) for the same initial conditions.<sup>25</sup> As seen from the spectra, at 32474.433  $cm^{-1}$  (307.935 nm) the  $Q_1(1)$  is the strongest line to pump in the portion of the  $A^2\Sigma^+ (v' = 0) \leftarrow X^2\Pi_i (v'' = 0)$  OH band that is accessible by the dye laser. The dissociated  $H_2O$  fraction is calculated in the limit of weak absorption ( $\sigma n_i L < 1$ ) when Beer-Lambert law<sup>26</sup> is equated to the energy loss of the laser due to absorption for all levels:

$$(n_{di})/(n_i) = (\sigma_i E)/(h\nu A) \quad (1)$$

where in the  $i^{\text{th}}$  vibrational level,  $n_i$  is the number density of water,  $n_{di}$  is the number density of dissociated water,  $\sigma_i$  is the absorption cross section,  $E$  is the laser pulse energy,  $h$  is Planck’s constant,  $\nu$  is the frequency of light,  $L$  is the length of the  $H_2O$  region through which the laser beam travels and  $A$  is the area of the laser beam. At room temperature (300 K), all the  $H_2O$  molecules are in the ground vibrational state with three fundamental frequencies ( $\nu_1, \nu_2, \nu_3$ ) for three modes: symmetric stretch ( $\nu_1 = 3651.7$   $cm^{-1}$ ), symmetric bend ( $\nu_2 = 1595.0$   $cm^{-1}$ ), and asymmetric stretch ( $\nu_3 = 3755.8$   $cm^{-1}$ ). For 193 nm, the ground state

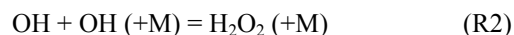
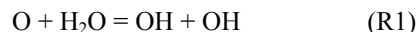
(0, 0, 0) absorption cross section is small,<sup>22</sup>  $8 \times 10^{-22}$  cm<sup>2</sup> and leads to about 1% dissociation of H<sub>2</sub>O vapor in room air for typical experimental conditions (8 mJ/pulse, 20 ns, 0.5 mm diameter laser beam,  $\sim 0.205$  GW/cm<sup>2</sup> irradiance). This relatively low (orders of magnitude) pulse energy (as compared to typical nonlinear methods with  $\sim 50$  GW/cm<sup>2</sup> irradiance<sup>17</sup>) can be very beneficial especially in measurements that might be conducted near windows or in gases containing particles that might otherwise tend to break down (i.e. ionize) under the high laser irradiance levels that are required for excitation by nonlinear methods. For typical room air conditions of 24.4°C (297.4 K) and 40% RH, 1% dissociation of H<sub>2</sub>O leads to a number density of  $\sim 3 \times 10^{15}$  OH molecules/cm<sup>3</sup> (125 PPM). The OH tag is formed immediately by 193 nm photodissociation from the ArF excimer laser pulse. The flow tag's formation is limited only by the lasers' pulse width, which is  $\sim 20$  ns. This short formation time makes HTV amenable, but not limited, to high-speed flows, where the time delay between write and read lasers may be  $< 1$   $\mu$ s.

The strength of the OH tag "read" signal depends on the initial mole fraction of H<sub>2</sub>O vapor present in the ambient air (related to RH and temperature), the delay time between the write and read laser pulses and the molecular diffusion that takes place at room temperature for the OH molecule. A series of single shot images of the experimental flowfield (air jet) were taken to address the effect of delay time on the OH tag signal strength. The signal of a typical laser line segment in the HTV grid was integrated and averaged at various times to determine the decay of the integrated signal. This value is independent of the diffusion rate. A value for background (fairly constant from shot-to-shot) was subtracted from a corresponding total signal value to yield experimental points on the curve as shown in Fig. 3.

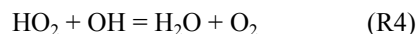
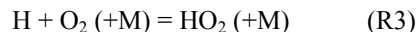
### **OH Tag Lifetime Predictions**

To predict the lifetime of the low temperature OH tag, the CHEMKIN II thermodynamic database and the SENKIN chemical kinetics solver<sup>27</sup> are used with an air chemistry mechanism consisting of a set of 109 reversible reactions (27 species) as previously shown.<sup>9</sup> A constant pressure, adiabatic system was simulated that initially contains equilibrium humid air mixture to which is added a certain amount of OH and H photoproducts. As calculated above,  $\sim 1\%$  of ambient H<sub>2</sub>O vapor (40% relative humidity, 297 K) is photodissociated into  $\sim 125$  PPM of OH and H atoms by the ArF write laser. Fig. 3 shows a comparison between the SENKIN predictions for OH concentration (either with 0- or 200 PPM of initial O atoms concentration) and experimentally determined OH tag signal intensity that is both normalized and plotted as a function of

delay time between the write and read lasers. The rates of two significant OH recombination pathways:



were modified from their previous values,<sup>18</sup> to better model both low- and high-temperature air situations. With no O atoms, OH is rapidly depleted primarily via the chain sequence:



where a fast formation of HO<sub>2</sub> (R3) leads to OH depletion (R4). However, a small amount of O atoms (200 PPM) will be present based on the expected  $\sim 0.05\%$  O<sub>2</sub> dissociation by the broadband ArF laser. With the O atoms present, there is a much better comparison between the simulation and experiment. The initial O atom concentrations were varied over a wide range (100 - 4100 PPM) of input conditions to the SENKIN solver without any appreciable changes in the OH depletion rates. The initial presence of O atoms depletes HO<sub>2</sub> and additionally regenerates OH through:

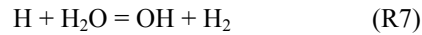
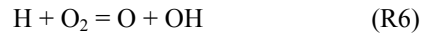


Slight underprediction of the experimental results by the mechanism could be attributed to uncertainties in both the initial conditions as well as rate constant parameters, notably for R4, which has the greatest uncertainty. Detailed description of the air chemistry mechanism and its reactions (with the appropriate reactions references) is given elsewhere.<sup>9</sup>

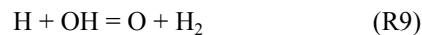
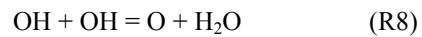
To determine the effect of temperature on the OH tag lifetime, the OH time histories were simulated for several different initial temperatures (see Fig. 3 inset), ranging from 297 K to 1500 K, where constant initial mole fractions of OH are assumed (125 PPM) and with 200 PPM of O. While low temperatures ( $< 500$  K) have minimal effect on initial rise in OH concentration, it is observed that at higher temperatures ( $> 600$  K) additional amounts of OH are produced at very short delay times ( $< 10$   $\mu$ s). These results agree with previously demonstrated SENKIN simulations of high-temperature combustion environments.<sup>19</sup> All temperature cases tend to fall back to the equilibrium OH concentrations (not shown) as delay time increases significantly especially for the higher temperature cases. The inset in Fig. 3 shows results only for the first 100  $\mu$ s of OH time histories since typical HTV write/read delay times are in that range (0-100  $\mu$ s).

To determine the lifetime of the OH tag in the hydrogen-air combustion hot products, the SENKIN chemical kinetic solver<sup>27</sup> was used to calculate the chemical composition as a function of time under constant enthalpy and pressure conditions. These conditions would be typical of those encountered in the atmosphere or in test facilities. Here we use the CHEMKIN library and a shortened hydrogen-air mechanism from GRIMECH 2.11 that consisted of 69 reactions.<sup>27,28</sup> Since the calculations are in a carbon free environment, the carbon bearing reactions were not considered. The complete reaction mechanism is published elsewhere.<sup>29</sup>

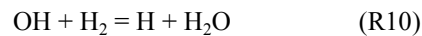
The results of the SENKIN calculations for H<sub>2</sub>O photodissociation in lean and rich streams of H<sub>2</sub>-air combustion products at atmospheric pressure (1 atm) were used to study the OH lifetimes in these flames. Here we have assumed the initial amount of 1% H<sub>2</sub>O photodissociation. For a typical laser beam (15 mJ, 0.5 mm dia.) this is a conservative estimate. For times longer than 10 ms, the initial OH recombines to its equilibrium concentration. For both the lean flames ( $\phi = 0.43$ , and  $0.69$ ), the OH tag is produced very quickly (20 ns) and lasts for  $\sim 1$  ms. In these lean flames the concentration of the OH is enhanced over the amount initially produced by the photodissociation of H<sub>2</sub>O. The increase of OH (in the short time scale of 1  $\mu$ s) is attributed mostly to the reactions:



while the depletion pathways for OH are through the reactions:



In very fuel rich conditions, the excess H<sub>2</sub> fuel quickly consumes OH through (R10) forming water and atomic hydrogen:



A detailed description of the chemical kinetics and of the analyses is published elsewhere.<sup>19,28</sup>

### **HTV Imaging in an Air Jet**

Figure 4a shows the experimental schematic and Fig. 5 shows HTV flow tagging results in an air jet created by a small nozzle (1.8 mm dia.) emanating vertically into a quiescent surrounding environment (Fig. 1). Figure 5a shows a typical instantaneous image

of the HTV grid for a write-read delay of 0  $\mu$ s, thus providing initial locations for the grid lines' cross points in the flow. Figure 5b shows another image of the same HTV grid displaced after a 2  $\mu$ s delay. This is for a location immediately downstream from the nozzle's exit (10 mm) near the jet's centerline. Based on the initial and final locations of these grid lines and the write-read time delays, one can establish velocity vector profiles. The images were taken in an under-expanded jet with velocities as high as 230 m/s (in the center, closest to the jet's exit). Slight variations in tag lines' intensity are attributed to unequal splitting of laser beam, non-uniform intensity profile of the dye and excimer lasers, system alignment, and possible beam transmission problems. The darker "dots" were images of elastically scattered particles in the flow mostly due to Lorentz-Mie scattering close to the pump wavelength ( $\sim 308$  nm) of the read dye laser. Since the fluorescence emission is mostly from  $v' = 0$  due to the ( $0 \leftarrow 0$ ) pumping of OH at  $\sim 308$  nm, the fluorescence light is very close to the laser wavelength. This elastic particle scattering can be minimized (or even avoided) by using, say,  $A^2\Sigma^+ (v' = 1) \leftarrow X^2\Pi_i (v'' = 0)$  OH excitation at  $\sim 285$  nm to read the HTV grid, and imaging only ( $1 \rightarrow 1$ ) emission at 308 nm.

The HTV grids shown in Fig. 5 were analyzed using commercial optical tracking software (DaVis 6.0 Stereo PIV/PTV, by LaVision, GmbH). The velocity field results are shown in Fig. 6. This method relies on a short-pixel defined structure that uses iterative multi-grid passes together with deformed interrogation windows adjusting to the local velocity gradient. This enhances the robustness and precision of the method especially in high gradient flowfields. Another feature is the use of FFT-correlations with short evaluation times. Domain transformation is replaced by first-order approximation of the local displacement distribution. This results in matching between regions where the continuum deformation is accounted for, in terms of translation, rotation, shearing, and dilatation. In addition, the displacements are locally independent, which means that a single "bad" velocity vector can be eliminated at a later time. Since this method correlates flow structures rather than intensity gradients, one can really compute the true (projected) 2-D flow field displacement. The method can also track the gridlines between the grid's crossing points to provide additional velocity vectors. Detailed descriptions of similar algorithms have been published elsewhere.<sup>30,31</sup> Note that the optical tracking method can give spurious data as shown in Fig. 6. The software is tracking the dust particles in the air as shown in the images in Fig. 5. This is due to the elastic particle scattering problem as already discussed.

### HTV Imaging in H<sub>2</sub>-Air Flames

Figure 4b shows the experimental schematic of HTV measurements in an H<sub>2</sub>-air flame whose instantaneous images are shown in Fig. 7. A Hencken multi-element fuel flame diffusion burner (50 mm x 50 mm) was used where premixed H<sub>2</sub> and air were flowed in the vertical direction. A short delay time (10 μs) between the 193-nm write ArF excimer and the 308-nm read dye laser was used in a lean flame ( $\phi = 0.39$ ). Figure 7a shows the undisplaced 7 x 7 grid and its displacement is shown in Fig. 7b. The images were taken at ~ 45 mm above the burner's surface, along its centerline. The burner's reacting flowfield is wide enough to show the complete 7 x 7 HTV grid lines resulting in 49 separate unambiguous cross points. The clean (filtered) flow from the Hencken burner has no particles that could cause Lorentz-Mie scattering as seen in the low temperature HTV images in Fig. 5. The images from Fig. 7 were analyzed using again the DaVis 6.0 software and the resulting displacement vectors are shown in Fig. 8. If one considers the delay time (10 μs) between the two images, then a typical velocity vector can be computed (as shown in lower left corner in Fig. 8). A correlation size of 128 x 128 pixels was used with a 75% overlap. Curvature effect can be seen on both sides of the axial line of the burner and could be attributed to possible temporal flow changes. The background color shows the displacement in the horizontal x-axis. Displacements in the negative x-dir. are shown in blue, and displacements in the positive x-dir. are shown in red.

### Conclusions

A tunable 193-nm ArF excimer laser and an Nd-YAG pumped tunable 308-nm frequency-doubled dye laser are used for HTV flow tagging in room air- and high-temperature reacting flowfields. New compact grid forming optics are developed that form a 7 x 7 optical grid. The ArF excimer produces a grid of OH molecules that is displaced by the interrogated flowfield and imaged by the dye laser. The OH grid is created via a single-photon process that yields very long lines (>50 mm), compared to those generated by non-linear processes. The dye laser accesses the strong Q<sub>1</sub>(1) line at  $32474.433 \text{ cm}^{-1}$  (307.935 nm) in the  $A^2\Sigma^+$  ( $v' = 0$ ) ←  $X^2\Pi_i$  ( $v'' = 0$ ) OH band that compensates for the relatively weak 193-nm photodissociation cross-sections of ground vibrational state H<sub>2</sub>O. A multiline grid is used to demonstrate the feasibility of multipoint nonintrusive instantaneous velocity measurements at various temperatures and velocities. The HTV method could be viewed as the nonintrusive instantaneous molecular diagnostic method of choice in either low- or high-temperature flowfields at atmospheric or higher pressures with variable flow speeds.

### Acknowledgements

The authors gratefully acknowledge the support of NASA-Glenn (grant NAG3-1984, Dr. R. Seasholtz, technical monitor), BMDO-ARO (DURIP award DAAG55-98-1-0197, Dr. D. Mann, technical monitor), and AFOSR (DURIP award F49620-99-1-0120, Dr. J. Tishkoff, technical monitor). The authors thank Arnold Engineering Development Center (AEDC), Tennessee, for use of their ArF excimer laser and for their support under Sverdrup/AEDC Group Contract # T01-55. The technical assistance of Dr. B. Wieneke (LaVision, GmbH) with image processing is gratefully acknowledged.

### References

1. Doebelin, E. O. *Measurement Systems: Applications and Design*. McGraw-Hill, New York, 1996.
2. Measures, R. M., *J. Appl. Phys.* **39**, 5232 (1968).
3. Zimmermann, M. and Miles, R. B., *Appl. Phys. Lett.* **37**, 885 (1980).
4. McDaniel, J. C., Hiller, B., and Hanson, R. K., *Opt. Lett.* **8**, 51 (1983).
5. Marinelli, W., Kessler, W. J., Allen, M. G., Davis, S. J., and Arepalli, S., *AIAA Paper 91-0358*, 29<sup>th</sup> AIAA Aerospace Sciences Meeting and Exhibit, Reno, NV (1991).
6. Paul, P. H., Lee, M. P., and Hanson, R. K., *Opt. Lett.* **14**, 417 (1989).
7. Seasholtz, R. G., Zupanc, F. J., and Schneider, S. J., *J. Prop. Power* **8**, 935 (1992).
8. Forkey, J. N., Finkelstein, N. D., Lempert, W. R., and Miles, R. B., *AIAA J.* **34**, 442 (1996).
9. Ribarov, L. A., Wehrmeyer, J. A., Pitz, R. W., and Yetter, R. A., *Appl. Phys. B.* **72**, 175 (2002).
10. Santoro, R. J., Pal, S., Woodward, R. D., and Schaaf, L., *AIAA Paper 2001-0748*, 39<sup>th</sup> AIAA Aerospace Sciences Meeting and Exhibit, Reno, NV (2001).
11. Maurice, M. S., *AIAA J.*, **30**, 376 (1992).
12. Mazumder, M. K. and Kirsch, K. J., *Appl. Opt.* **14**, 894 (1975).
13. Durst, F., Melling, A., and Whitelaw, J. H. *Principles of Laser-Doppler Anemometry*. Academic Press, London, U. K., 1976.
14. Gomez, A. and Rosner, D. E., *Comb. Sci. Techn.* **89**, 335 (1993).
15. Talbot, L., Cheng, R. K., Shefer, R. W., and Willis, D. R., *J. Fl. Mech.* **101**, 737 (1980).
16. Boedecker, L. R., *Opt. Lett.* **14**:473 (1989).
17. Miles, R. B. and Lempert, W. R., *Annu. Rev. Fluid Mech.* **29**, 285 (1997).
18. Ribarov, L. A., Wehrmeyer, J. A., Batliwala, F., and Pitz, R. W., *AIAA J.* **37**, 708 (1999).
19. Wehrmeyer, J. A., Ribarov, L. A., Oguss, D. A., and Pitz, R. W., *Appl. Opt.* **38**, 6912 (1999).

20. Pitz, R. W., Wehrmeyer, J. A., Ribarov, L. A., Oguss, D. A., Batliwala, F., DeBarber, P. A., Deusch, S., and Dimotakis, P. E., *Meas. Sci. Tech.* **11**, 1259 (2000).
21. Seitzman, J. M. and Hanson, R. K., *AIAA J.* **31**, 513 (1993).
22. van Hemert, M. S. and van Harreveld, R., Private Communication (1999); also see *J. Chem. Phys.* **114**, 9453 (2001).
23. Bass, A. M. and Broida, H. P., *Nat. Bureau of Stand. Circ.* **541**, 1 (1953).
24. Dieke, G. H. and Crosswhite, H. M., *J. Quant. Spect. Radiat. Trans.* **2**, 97 (1962).
25. LIFBASE, Vers. 1.6, ([www.sri.com/cem/lifbase](http://www.sri.com/cem/lifbase)).
26. Eckbreth, A. C. *Laser Diagnostics for Combustion Temperature and Species*. Gordon and Breach, Amsterdam, 1995.
27. A.E. Lutz, A. E., Kee, R. J., and Miller, J. A., Sandia Report: SAND87-8248-UC-4 (1988).
28. GRIMECH Vers. 2.11, Release 11/3/95, CHEMKIN-II format ([www.gri.org](http://www.gri.org)).
29. Wehrmeyer, J. A., Ribarov, L. A., Oguss, D. A., and Pitz, R. W., *AIAA Paper 99-0646*, 37<sup>th</sup> AIAA Aerospace Sciences Meeting and Exhibit, Reno, NV (1999).
30. Fincham, A. and Delerce, G., *Exp. in Fluids [Suppl.]* **29**, 13 (2000).
31. Scarano, F. and Reithmuller, M. L., *Exp. in Fluids [Suppl.]* **29**, 51 (2000).

### Figures

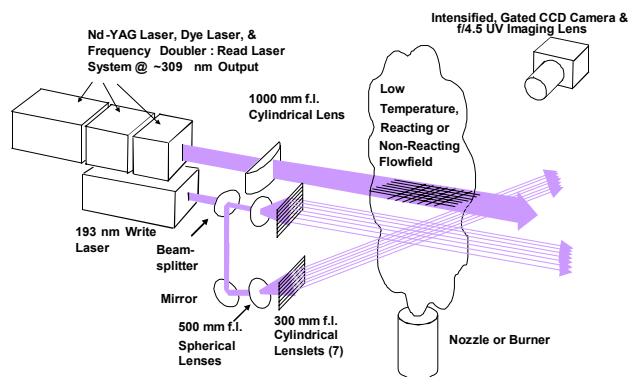


Fig. 1. Schematic of the HTV experimental system.

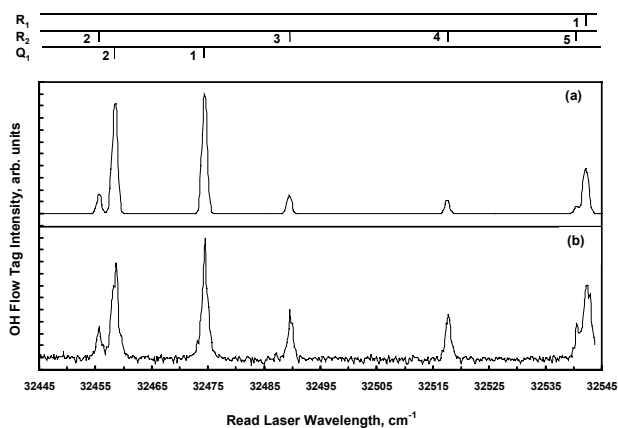


Fig. 2. Room temperature (300 K) HTV LIF excitation spectra showing the strong  $Q_1(1)$  transition of the  $A^2\Sigma^+(\nu' = 0) \leftarrow X^2\Pi_i(\nu'' = 0)$  OH band. Curves are normalized to the  $Q_1(1)$  line showing (a) simulation by LIFBASE<sup>25</sup> (assumed: 1  $\text{cm}^{-1}$  linewidth, Gaussian lineshape), and, (b) experimental spectrum.

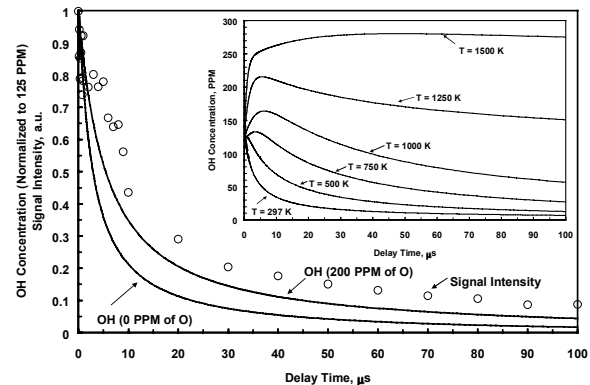


Fig. 3. Average HTV signal intensity and OH concentrations (SENKIN<sup>27</sup> predictions with- and without O atoms) curves as function of delay time between write and read lasers. Inset shows OH time histories (125 PPM of initial OH and 200 PPM of initial O mole fraction) at constant pressure (1 atm) and various initial temperatures.

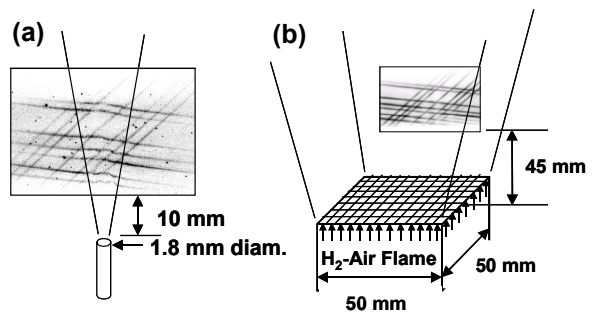
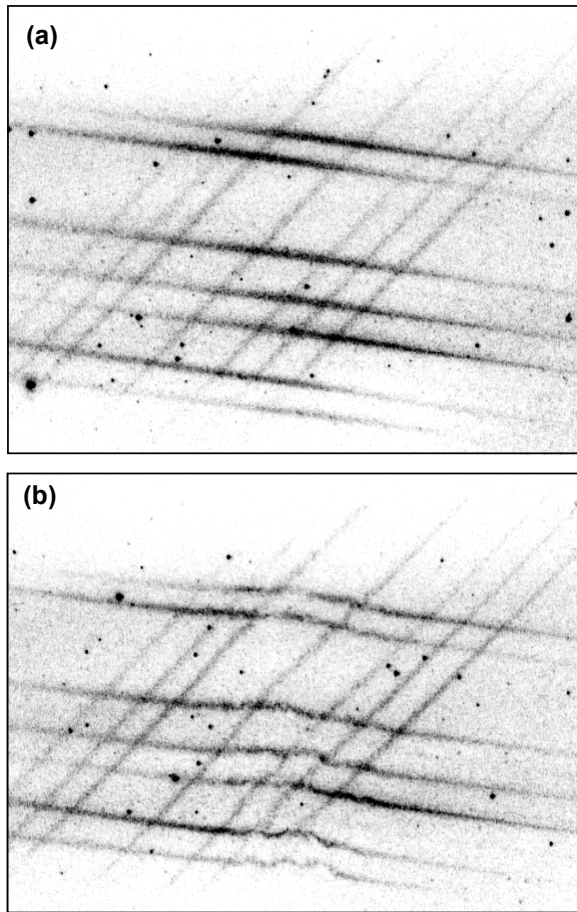
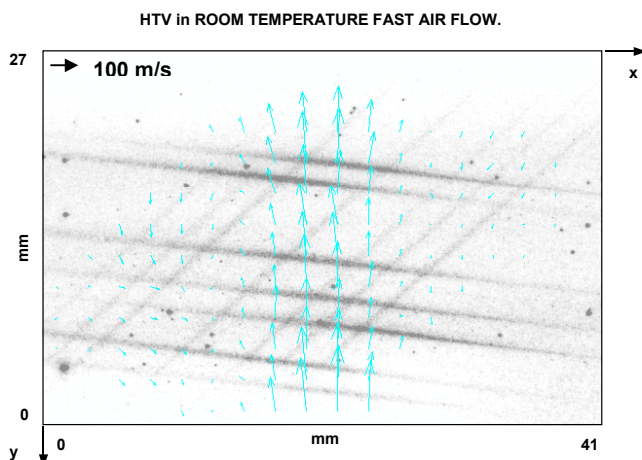


Fig. 4. Schematics (not to scale, but with proper dimensions) of experimental HTV measurements in (a) small air jet nozzle, and (b) Hencken burner for the images shown in Fig. 5 and Fig. 7 respectively.



**Fig. 5.** Single-pulse OH fluorescence images of a 7x7 optical grid from H<sub>2</sub>O photodissociation taken in under-expanded high-speed air jet. Write/read delays: (a) 0 μs, (b) 2 μs. Dimensions: 41 mm length, 27 mm height in both images.



**Fig. 6.** Analysis of HTV images shown in Fig. 5 to yield velocity field data. The HTV grids were analyzed using the DaVis 6.0 stereo PIV/PTV software (LaVision, GmbH).

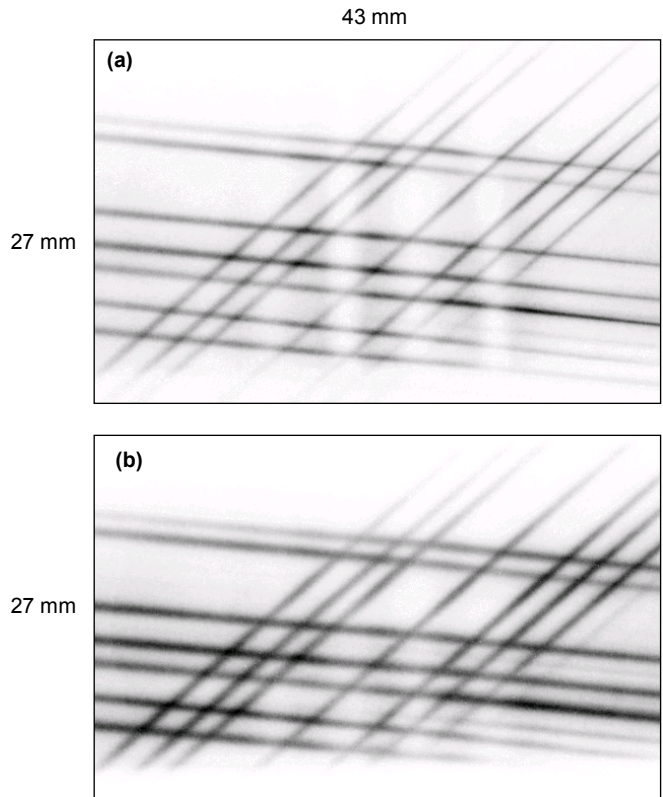


**Fig. 7.** Single-pulse instantaneous HTV images of the 7x7 optical grid taken in a lean ( $\phi = 0.39$ ) H<sub>2</sub>-Air flame issuing vertically in both images. Write/read delays: (a) 0 μs, (b) 10 μs.

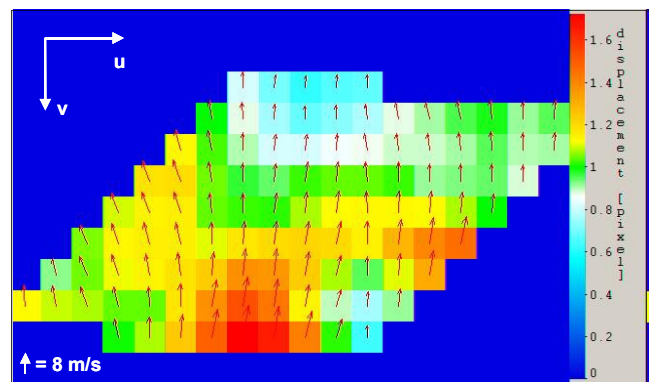


**Fig. 8.** Analysis of HTV images shown in Fig. 7 to yield velocity field data. The HTV grids were analyzed (correlation size: 128 x 128 pixels, 75% overlap) using the DaVis 6.0 stereo PIV/PTV software (LaVision, GmbH).